Structural and Mechanistic Insights into Caffeine Degradation by the Bacterial *N*-Demethylase Complex

Jun Hoe Kim [1], Bong Heon Kim [1], Shelby Brooks [2], Seung Yeon Kang [1], Ryan M. Summers [2] and Hyun Kyu Song [1]

*1 - **Department of Life Sciences,** Korea University, 145 Anam-ro, Seongbuk-gu, Seoul 02841, Republic of Korea*
*2 - **Department of Chemical and Biological Engineering,** The University of Alabama, Tuscaloosa, AL 35487, USA*

***Correspondence to Hyun Kyu Song:** hksong@korea.ac.kr*
https://doi.org/10.1016/j.jmb.2019.08.004

Abstract

Caffeine, found in many foods, beverages, and pharmaceuticals, is the most used chemical compound for mental alertness. It is originally a natural product of plants and exists widely in environmental soil. Some bacteria, such as *Pseudomonas putida* CBB5, utilize caffeine as a sole carbon and nitrogen source by degrading it through sequential *N*-demethylation catalyzed by five enzymes (NdmA, NdmB, NdmC, NdmD, and NdmE). The environmentally friendly enzymatic reaction products, methylxanthines, are high-value biochemicals that are used in the pharmaceutical and cosmetic industries. However, the structures and biochemical properties of bacterial *N*-demethylases remain largely unknown. Here, we report the structures of NdmA and NdmB, the initial N_1- and N_3-specific demethylases, respectively. Reverse-oriented substrate bindings were observed in the substrate-complexed structures, offering methyl position specificity for proper *N*-demethylation. For efficient sequential degradation of caffeine, these enzymes form a unique heterocomplex with 3:3 stoichiometry, which was confirmed by enzymatic assays, fluorescent labeling, and small-angle x-ray scattering. The binary structure of NdmA with the ferredoxin domain of NdmD, which is the first structural information for the plant-type ferredoxin domain in a complex state, was also determined to better understand electron transport during *N*-demethylation. These findings broaden our understanding of the caffeine degradation mechanism by bacterial enzymes and will enable their use for industrial applications.

Introduction

Many bacteria have enzymes that degrade environment-derived exogenous compounds, such as single aromatic rings or multiple benzene rings fused to polycyclic aromatic hydrocarbons [1]. They are widely dispersed in the environment and have detrimental biological effects, including toxicity and mutagenicity [2,3]. Rieske nonheme iron oxygenases (ROs) catalyze the initial oxygenation reaction of aromatic compounds by enantio- and regiospecific reactions [4,5]. The RO system is generally composed of a terminal oxygenase and one or two electron transfer components [6]. Like other oxygenases, RO substrate catalysis occurs by the incorporation of either one (monooxygenase) or both atoms (dioxygenase) of O_2 into the target site with the help of transition metals (iron, copper, or manganese) and organic cofactors (NAD[P]H, flavin) [7]. Recent biochemical and structural studies have revealed that ROs exhibit an α3 or α3β3 configuration [6–11]. The α-subunit is divided into two structural domains by role; the N-terminus contains a Rieske [2Fe–2S] cluster for accepting electrons from other electron transfer components, while the ligand-binding C-terminus has a nonheme iron center for substrate oxidation. The distance between the Rieske cluster and the mononuclear iron is ~45 Å within a subunit but is ~12 Å through the neighboring subunit; therefore, quaternary arrangements are indispensable for proper electron transfer [4]. No functional role has been attributed to the β-

subunit, and only a structural role has been demonstrated; however, the β-subunit can influence substrate specificities in some ROs [12–14]. Thus far, more than 130 RO families have been reported, among which naphthalene dioxygenase and biphenyl dioxygenase are the most extensively studied [8,9,15–19].

The soil bacterium *Pseudomonas putida* CBB5 can use caffeine (1,3,7-trimethylxanthine) as a sole carbon and nitrogen source by degrading it to xanthine via sequential *N*-demethylation [20]. Recent studies have reported a novel type of RO in *P. putida* CBB5, consisting of NdmA, NdmB, and NdmC, which specifically detach methyl groups from the *N*-1, *N*-3, and *N*-7 positions of methylxanthine derivatives, respectively (Fig. S1) [21,22]. A single formaldehyde is produced whenever one *N*-linked methyl group is detached, indicating that NdmA, NdmB, and NdmC are monooxygenases. The *N*-demethylation of caffeine to xanthine occurs via three steps; NdmA and NdmB catalyze the initial two steps of *N*-demethylation, and the intermediate product, 7-methylxanthine, is further catalyzed to xanthine by an unusual RO-reductase complex, the NdmCDE heterotrimer [23]. Intriguingly, NdmCDE has an enigmatic domain architecture; NdmC contains the ligand-binding domain, and the remaining Rieske domain must be nonfunctional because the metal coordinating residues are not conserved. Instead, a potentially functional Rieske domain is located at the N-terminus of NdmD. This unique feature has never before been reported in the RO family. In addition to the N-terminal Rieske domain, NdmD is composed of a flavin mononucleotide (FMN)-binding domain, an NADH-binding domain, and a C-terminal plant-type ferredoxin domain. The plant-type ferredoxin domain coordinates the iron–sulfur cluster with four cysteine residues; meanwhile, the Rieske-type ferredoxin domain uses two cysteine and two histidine residues. NdmD plays the role of a reductase, which transfers electrons from NADH to NdmA and NdmB for oxygen activation. Another component, NdmE, has no discernable function, but exhibits high structural similarity to many glutathione-*S*-transferases. Expression without all three components of NdmCDE has been reported to decrease the solubility of the whole protein complex, suggesting that NdmE facilitates complex formation by structural alignment [23]. These *N*-demethylases have broad specificities for purine alkaloids and are classified as a novel RO family, but their structural and biochemical properties are still largely unknown.

Here we report the crystal structures of *N*-demethylase A and B from *P. putida* CBB5. By comparing the apo- and substrate-bound structures, we investigate the *N*-demethylation mechanism and regio-specificities for substrates. In addition, we reveal that *N*-demethylase A and B prefer to produce a heterohexamer with the α3α′3 configuration (NdmAB), which is a novel type of RO oligomerization state. The improved efficiency of NdmAB for serial caffeine *N*-demethylation is confirmed by biochemical studies. Moreover, from the complex structure of the NdmD ferredoxin domain with NdmA, we provide information about the interactions and the electron transport pathway between RO components during *N*-demethylation. These findings provide the substrate specificity and reaction mechanism of bacterial *N*-demethylation, and they are also potentially useful for many caffeine- and other methylxanthine-related industrial applications [24–28].

Results and Discussion

Structures of NdmA and NdmB

Since the oligomeric states of NdmA and NdmB have not been characterized in solution, they were analyzed by size-exclusion chromatography associated with small-angle x-ray scattering (SEC-SAXS) and multi-angle light scattering (SEC-MALS) methods, together with symmetry mates from crystal structures (Figs. 1a and S2 and Table S1). NdmA and NdmB were expressed as homohexamers (α6), with the dimer of trimer configuration by 3-fold symmetry on the longitudinal axis and 2-fold symmetry on the horizontal axis (Fig. 1b). The crystal structures of NdmA and NdmB were determined at 1.95 and 2.10 Å resolution, respectively

Fig. 1. Solution and crystal structures of NdmA and NdmB. (a) SAXS envelopes of NdmA (top, cyan), NdmB (middle, magenta), and the NdmAB complex (bottom, wheat). Each protein is fitted into the map in its hexameric configuration. (b) Surface representation of the hexameric NdmA crystal structure. Each subunit is colored differently. (c, d) Cartoon representation of monomeric NdmA (c) and NdmB (d). Yellow and magenta regions are responsible for the Rieske domains, and green and cyan regions are the SRPBCC domains. (e) Topology diagram of NdmA, which is colored as in panel c. Asterisks denote the cofactor-coordinating residues; orange asterisks denote the [2Fe–2S] cluster, and purple asterisks indicate the nonheme iron center. (f, g) Two histidine and two cysteine residues denote the coordinating [2Fe–2S] cluster in the Rieske domains (f), and two histidine and one aspartic acid residues indicate the coordinating nonheme iron center in the SRPBCC domains (g). The structures of NdmA and NdmB are superposed, and the residues coordinating metal atoms are labeled with subscripts A and B for NdmA and NdmB, respectively.

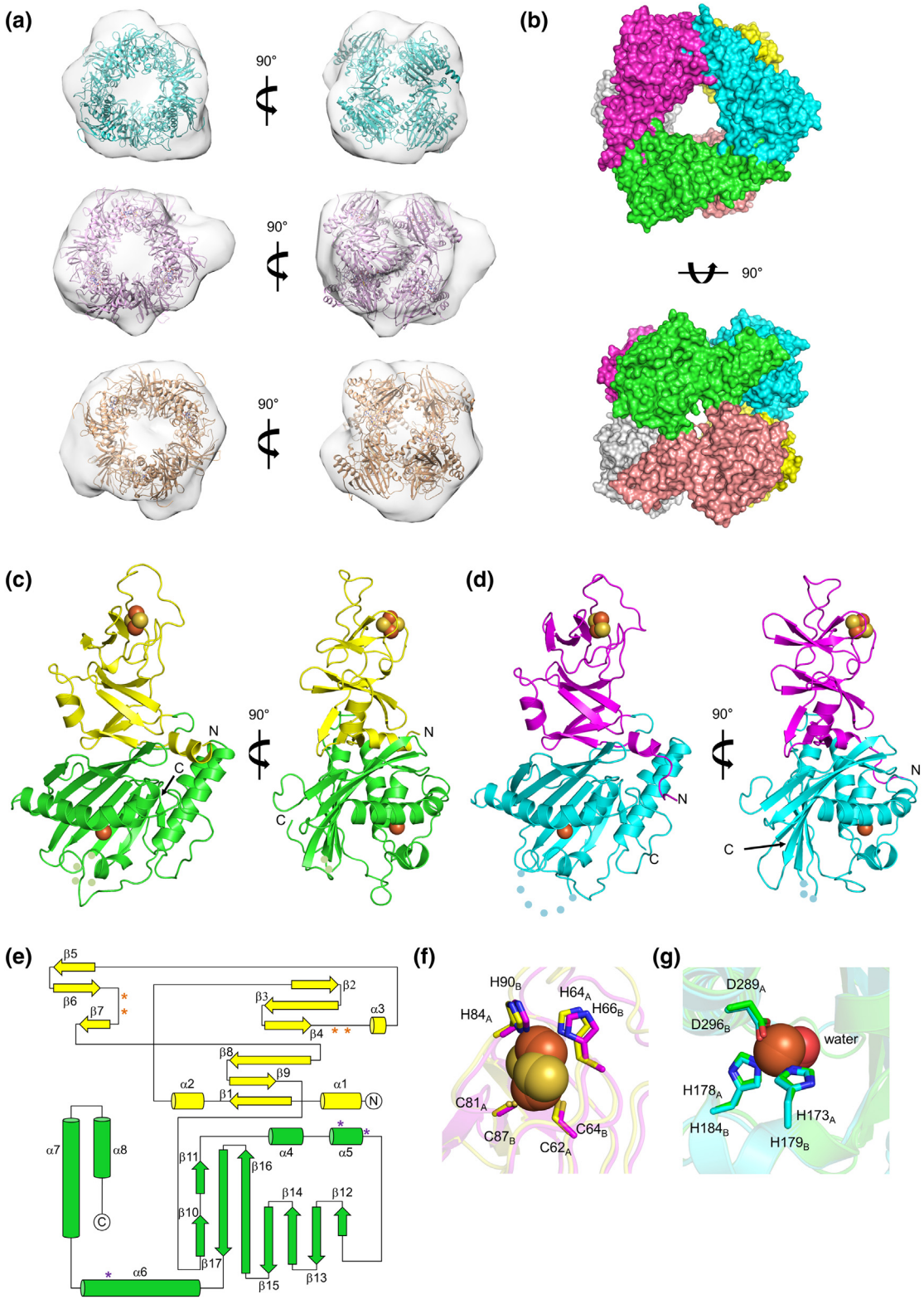

(Table S2), showing a structural similarity between monomers of 0.898-Å root-mean-square deviations (using 311 matching Cα atoms) and 1.215 Å between hexamers (using 1866 matching Cα atoms).

Both enzymes can be divided into two domains: N-terminal Rieske-type [2Fe–2S] cluster domains and C-terminal ligand binding domains, also known as the START/RHO_alpha_C/PITP/Bet_v1/CoxG/CalC (SRPBCC) domain (Fig. 1c,d). There were

three α-helices and nine β-strands in the Rieske domain, and five α-helices and eight β-strands in the SRPBCC domain (Fig. 1e). However, in NdmB, the α3 helix was missing and was replaced by a loop region. Similar to the typical Rieske-type cluster, the [2Fe–2S] cluster was coordinated by two cysteine and two histidine residues located in the loop regions between β4 and α3 and between β6 and β7 (Figs. 1f and S3a, b). The nonheme iron center formed an octahedral arrangement with two histidines, one aspartic acid, and water molecules on the catalytic face (Figs. 1g and S3c, d). The distance of the Rieske [2Fe–2S] cluster to the nonheme iron was 44.7 Å within the monomer, but only 12.1 Å between the neighboring subunits, which was in agreement with structural information of other Rieske non-heme oxygeneases [4]. Therefore, this quaternary structure is needed for proper electron transport. The loop regions between β13 and β14 were invisible in both the NdmA and NdmB structures due to their high flexibility (Fig. S3e, f). In the previous dicamba monooxygenase study, the corresponding region to the invisible loops of NdmA and NdmB was involved in dicamba binding by changing the open conformation to closed form [7,11].

The overall structure of NdmA exhibited high similarity to several other known ROs, such as dicamba monooxygenase (PDB ID: 3GOB, Z = 30.5) [7], 3-ketosteroid-9-α-hydroxylase 5 (PDB ID: 4QDC, Z = 24.8) [29], 2-oxoquinoline-8-monooxygenase (PDB ID: 1Z01, Z = 23.7) [30], biphenyl 2,3-dioygenase (PDB ID: 2GBW, Z = 18.1) [31], and a putative aromatic-ring hydroxylating dioxygenase (PDB ID: 3N0Q, Z = 17.0) (Fig. S4). The SRPBCC domains exhibited relatively variable structures compared to the Rieske domains, depending on their roles and substrate selectivity. In particular, the peripheral regions of the SRPBCC domain were deviated more among the structurally homologous proteins (Fig. S4), and interestingly, they correspond to the interaction interface between trimer and trimer, which is unique for the NdmAB architecture (see the Heterohexamer formation of NdmAB section for details).

Substrate recognition by *N*-demethylases

To obtain the substrate-bound *N*-demethylase structures, caffeine (CF) and theophylline (1,3-dimethylxanthine; TP) were used for NdmA, and caffeine and theobromine (3,7-dimethylxanthine; TB) were used for NdmB. By soaking the protein crystals directly in a high concentration of chemical solution, caffeine- and theophylline-bound NdmA structures were obtained at 1.65 and 1.85 Å, respectively (Fig. 2 and Table S2). Both caffeine and theophylline were tightly bound to the substrate binding pocket of the SRPBCC domain (Fig. 2a, b, e). F168 formed a characteristic π–π bond with the purine backbone of caffeine, and the side chain atoms of F174, F223, L248, N282, V285, and F286 participated in hydrophobic interactions with caffeine (Fig. S5a). Compared with the apo structure, several residues were rotated for optimal interaction (Fig. 2i). In contrast to the robust binding mode of caffeine, the residues interacting with theophylline showed deviations depending on the subunits; for example, F174, L182, and F223 residues were observed indistinctly (Fig. S5b). The binding pocket was tightly closed via hydrophobic interactions between substrate and P219 on the loop between β13 and β14, which as mentioned above was missing in the apo structure (Figs. S3e, f and S6). Two water molecules located near the nonheme cobalt center make hydrogen bonded with caffeine. According to the structures, the distance from the water at the nonheme cobalt center to the N_1-methyl group was closer (3.52 ± 0.00 Å) than that of the N_3-methyl group (7.74 ± 0.04 Å) of caffeine (Fig. 2i). A similar tendency was also found in the theophylline bound structure, showing N_1- and N_3-methyl groups as far as 3.59 ± 0.07 and 7.84 ± 0.06 Å, respectively (Fig. 2j).

Despite much effort, we did not obtain substrate-bound structure of NdmB. Therefore, we analyzed the residues of NdmA, which are involved in the caffeine binding, and compared them with NdmB by sequence alignment (Fig. S7) to create a mutant NdmA that imitates the catalytic site of NdmB (hereafter referred to as $NdmA_{QL}$). For this, residues N282 and F286 in NdmA were mutated to Q289 and L293. To verify the altered *N*-demethylase activity, the caffeine and theobromine degradation abilities were examined (Fig. S8). In NdmA, more than half of the initial concentration of caffeine was consumed within 30 min, but the activity was reduced to less than 15% in the $NdmA_{QL}$ mutant. Instead, the degradation activity against theobromine increased almost 2-fold, meaning that the structure-guided mutation properly mimicked the catalytic core of NdmB. Although $NdmA_{QL}$ was in line with the degradation activity measured for NdmB, it seemed that another residue or region could affect the substrate selectivity or stabilization. Since the loop region between β13 and β14 changed the conformation depending on the presence of substrate, this possibility was tested by swapping the region with the counterpart of NdmB (residues from 207 to 221 of NdmA were replaced with residues from 213 to 227 of NdmB). The replacement decreased the protein solubility, suggesting a negative effect on the intramolecular network, but increased activity was observed by HPLC analysis (Fig. S8). We crystallized the loop region-swapped $NdmA_{QL}$ mutant; however, the crystal was weak and diffracted so poorly that it could not be structurally analyzed.

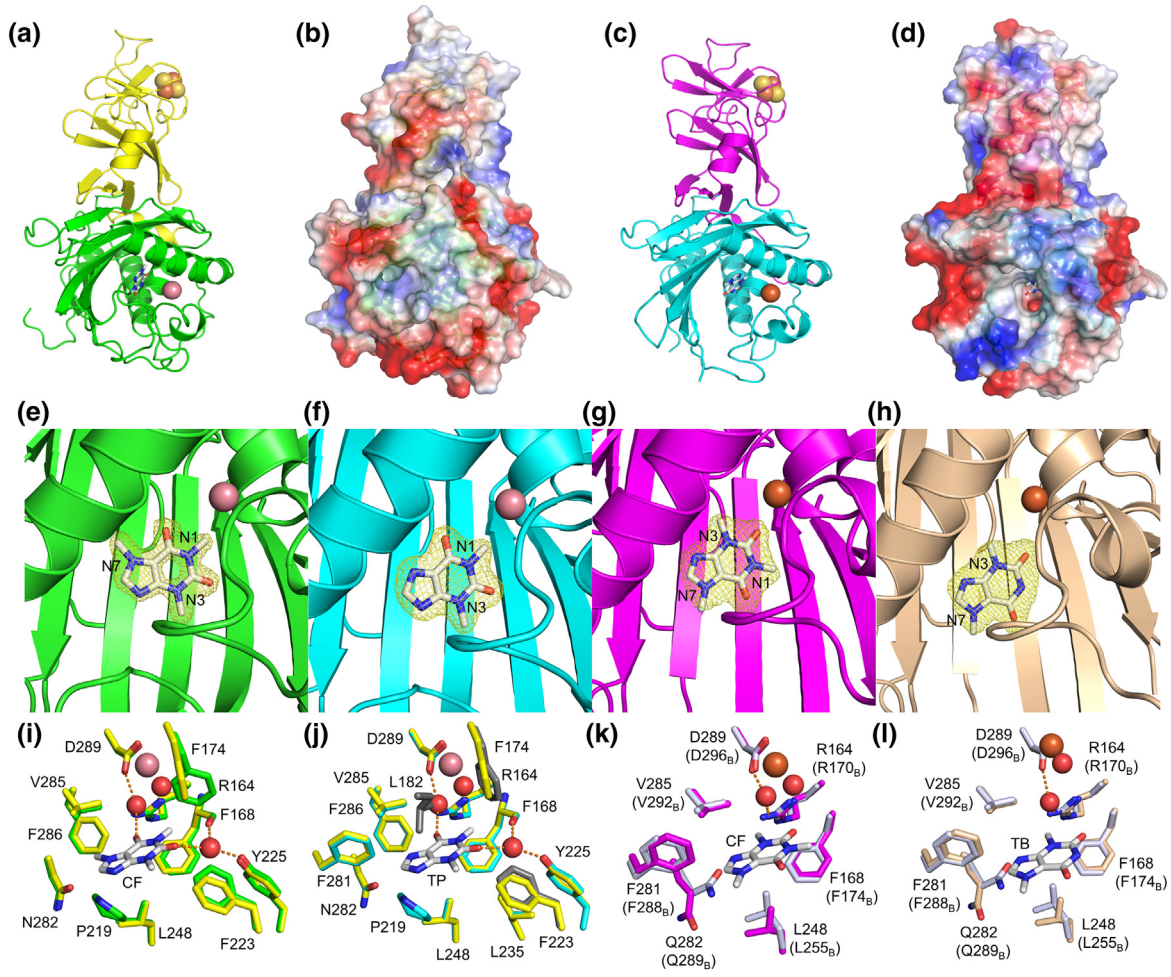

Fig. 2. Substrate-bound structures of NdmA and $NdmA_{QL}$, NdmB mimic mutant. (a, b) Overall structure of the NdmA-caffeine complex as a ribbon diagram (a) and as a transparent electrostatic potential surface (b). (c, d) Overall structure of the $NdmA_{QL}$-theobromine complex as a ribbon diagram (c) and as a transparent electrostatic potential surface (d). (e–f) Cartoon representations of NdmA-caffeine (e), NdmA-theophylline (f), $NdmA_{QL}$-caffeine (g), and $NdmA_{QL}$-theobromine complex structures (h). Nonheme iron centers are displayed as orange spheres (e, f) or salmon spheres for cobalt replacement (g, h). Note the reverse-orientated substrate binding between the NdmA and $NdmA_{QL}$ structures. Electron density maps are displayed as mesh in 1.0 σ contour. (i–l) Representations of substrate with interacting residues in stick models. Compared with the NdmA apo state structure (yellow), two water molecules, which are highly conserved in both caffeine (i)- and theophylline (j)-bound structures, adjust the substrate position. F174 and F223 are slightly rotated in the substrate-bound structure, and P219, which is located in a flexible loop region, is only shown in the complex state. The apo structure of NdmB (white) was compared with caffeine (k) and theobromine (l)-bound $NdmA_{QL}$ structures, and the corresponding residues of NdmB are shown in parenthesis with subscript B. Only a single water molecule is observed in the structure, but it is too far away to interact with the substrates. Q282 (Q289 in NdmB), which is expected to provide a different selection mechanism for NdmB, is rotated outward when the substrate is bound to allow space for the substrate. The residues showing perturbations depending on the subunits during interaction analysis are shown in gray.

Consequently, we solved the caffeine- and theobromine-bound structures by using NdmAQL instead of NdmB at 2.20 and 1.90 Å, respectively (Table S2 and Fig. 2c,d). To stop the enzyme reaction, an excess amount of substrates was applied to completely oxidize the nonheme iron center. The major difference compared with the substrate-bound NdmA structure was that caffeine and theobromine were located in the active site in the reverse orientation (Fig. 2k, l). F168 created a π–π bond with the backbone of the substrate, and the F281, V285, and L248 residues were involved in hydrophobic interactions. Q282, originally N282 in NdmA, was rotated to the outside, allowing space for substrate docking (Fig. 2k, l). Although a single water molecule was present around the nonheme iron

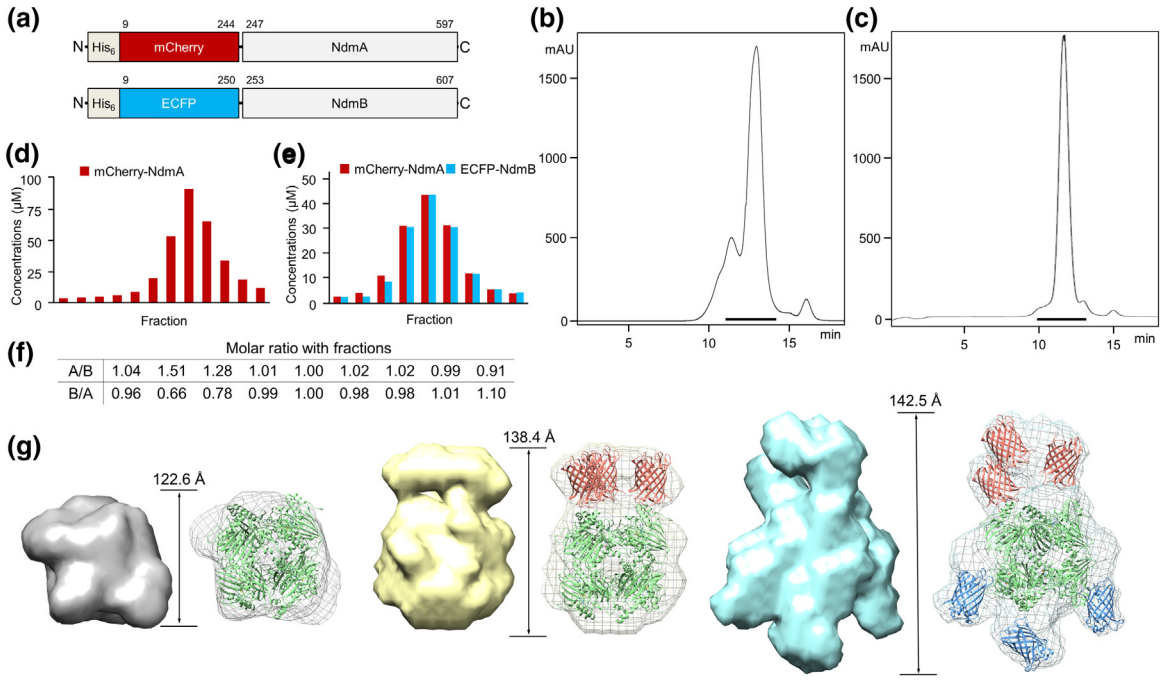

Fig. 3. Purification and stoichiometric analysis of fluorescent protein-labeled NdmAB. (a) Schematic of the fluorescent protein-labeled NdmA and NdmB constructs. (b, c) Size-exclusion chromatography profiles of mCherry-NdmA/NdmB (b) and mCherry-NdmA/ECFP-NdmB (c). (d, e) Quantification of mCherry-NdmA and ECFP-NdmB, which were fractionated from the peak (black bars in panels b and c). The concentrations were calculated from fluorescence emission values. (f) Molar ratios of fractionated mCherry-NdmA/ECFP-NdmB by size-exclusion chromatography. (g) SAXS envelopes of NdmAB (gray), mCherry-NdmA/NdmB (yellow), and mCherry-NdmA/ECFP-NdmB (cyan). Based on the known structures, each structure was modeled and fitted into the SAXS envelopes, which are represented as mesh.

center, it was too far distant to make a hydrogen bond with the substrate. Substrate interactions of L286, originally F286 in NdmA, were not detected during the structural analysis, potentially due to an insufficient imitation of the catalytic core of NdmB, which caused relatively loose binding of the substrates. The loop region was not closed states, unlike the NdmA-substrate structures (Fig. 2d).

Although the $NdmA_{QL}$-substrate complex structures did not perfectly reproduce the microenvironments of the NdmB-substrate state, the distance from the water molecule of the nonheme iron center to the N_3-methyl group of caffeine 4.72 ± 0.33 Å or theobromine at 3.79 ± 0.55 Å was obviously closer than that of the N_1-methyl group at 5.25 ± 0.05 Å. This feature was accomplished by the reverse-oriented binding of substrates, which allowed prioritized detachment of the N_3-methyl group. Taken together, the different substrate binding mode provides regio-specificities to NdmA and NdmB for proper *N*-demethylation.

Heterohexamer formation of NdmAB

To test the tendency of complex formation between NdmA and NdmB (referred to as NdmAB), we attempted to reconstitute NdmAB from the separately expressed NdmA and NdmB. There was no NdmA retained on the Ni-NTA column from the simple NdmA and His_6-NdmB mixture (Fig. S9a). However, when we performed the same experiment when NdmA and His_6-NdmB were coexpressed, both proteins were observed, indicating that they existed as an NdmAB complex (Fig. S9b). Both SEC-MALS and SAXS support the formation of a hexamer (Fig. S2c, f–h). Unfortunately, we were not able to crystallize the NdmAB complex. From these results, we concluded that heterohexamerization was preferred over homohexamerization, although the components were not easily swapped following the homohexamerization of each component.

To determine the stoichiometry of NdmAB, mCherry ($\lambda_{ex/em}$ = 590/620 nm) and ECFP ($\lambda_{ex/em}$ = 440/480 nm) were fused to the N-termini of NdmA and NdmB, respectively (Fig. 3a). After coexpression of mCherry-NdmA with NdmB or with ECFP-NdmB, the excess amounts of proteins that did not make the heterohexamer were discarded (Figs. 3b, c and S9c, d). The exact molar ratio of mCherry-NdmA to ECFP-NdmB was calculated from the fluorescence emission value (Fig. 3d–f and Fig. S9e, f), and the overall shapes of the complexes were analyzed by SAXS experiments (Figs. 3g and S10 and Table S1). Compared with NdmAB, a large additional blob was observed on the upside of the mCherry-NdmA/NdmB envelope. This

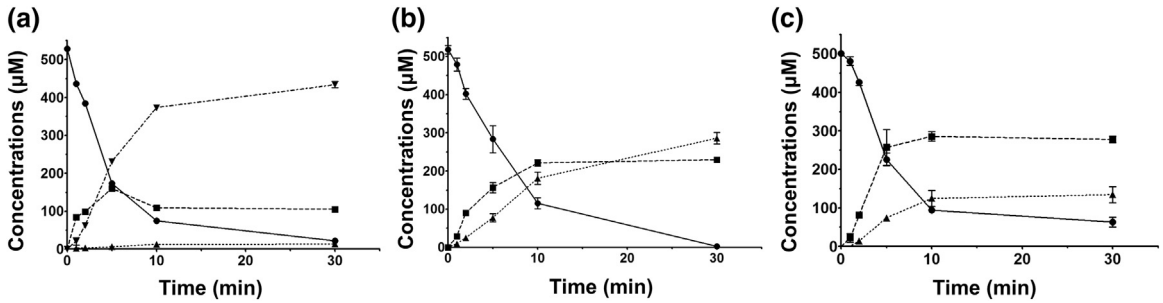

Fig. 4. HPLC analysis of caffeine consumption by NdmAB or a simple mixture of NdmA and NdmB. (a) Caffeine degradation by NdmAB in the presence of NdmCDE WT. The initial 500 ± 10 μM of caffeine was degraded by NdmAB to 22 ± 2 μM. The theobromine concentration reached 160 ± 5 μM within 5 min and 105 ± 7 μM at the end. N_3-demethylation of theobromine produced 13 ± 1 μM 7-methylxanthine, and NdmCDE finally produced 434 ± 8 μM xanthine. (b) Caffeine degradation by NdmAB in the presence of the NdmCDE mutant (NdmC H120A/D237A). The initial 518 ± 11 μM of caffeine was all N_1-demethylated by NdmAB, and 230 ± 4 μM of theobromine was produced. Theobromine was further N_3-demethylated to 286 ± 15 μM 7-methylxanthine, the final product. (c) Caffeine degradation by the mixture of purified NdmA and NdmB at a 3:3 molar ratio, instead of the NdmAB complex, in the presence of the NdmCDE mutant. The initial 501 ± 8 μM of caffeine was degraded to 63 ± 12 μM by the mixture. The mixture produced 278 ± 9 μM theobromine and 135 ± 21 μM 7-methylxanthine. Symbols: ●, caffeine; ■, theobromine; ▲, 7-methylxanthine; ▼, xanthine. Data represent the mean ± SEM of three independent experiments.

region was most likely occupied by triplicate N-terminal mCherry proteins. Moreover, in mCherry-NdmA/ECFP-NdmB, several blobs were observed under the opposite side of the mCherry position. Each region could be filled with an ECFP structure that was relatively dispersed compared with the mCherry models. From the SAXS analysis, we concluded that the stoichiometry of NdmAB heterohexamer is trimer-to-trimer (α3α′3).

Enzymatic efficiency of the α3α′3 configuration

To verify the advantages of the α3α′3 configuration, we performed the enzyme activity assays of NdmAB in comparison to the mixture of purified NdmA and NdmB. Because NdmCDE has the possibility of directly N_7-demethylating caffeine in a minor reaction, we generated an *N*-demethylase-inactive NdmCDE by mutating NdmC H120 and D237 to alanine to disrupt nonheme iron coordination. The enzyme kinetics of NdmA to caffeine and NdmB to theobromine was measured in the presence of inactive NdmCDE mutant (Table S3).

Because of their hexameric characteristics, the purified NdmA and NdmB were mixed with different molar ratios from 5:1 to 1:5 (Fig. S11). The caffeine consumption was increased as the portion of NdmA was elevated, and simultaneously, theobromine production also increased. Moreover, the least amount of 7-methylxanthine was observed at the highest ratio of NdmA due to the lowest molar ratio of NdmB. Conversely, when the portion of NdmB increased, caffeine turnover was reduced, but 7-methylxanthine production increased. When the NdmA portion was the lowest (1:5), production of 7-methylxanthine was less efficient because the caffeine turnover was too low. Therefore, the extreme stoichiometry was undesirable for sequential caffeine demethylation.

Then, we examined the activity of NdmAB for comparison with NdmA/NdmB mixture, which was simply blended in a 3:3 molar ratio. When the wild-type (WT) NdmCDE was used (Fig. 4a), most of the caffeine (>95%) was degraded by NdmAB within 30 min, while the theobromine concentration reached its peak point after 5 min and maintained the equilibrium concentration. The concentration of 7-methylxanthine was sustained below 5% by immediate degradation via the NdmCDE complex, which produced xanthine as a final product. As a result, the conversion from caffeine to xanthine was 87%. With the NdmCDE H120A/D237A mutant (Fig. 4b), NdmAB degraded more than 98% of caffeine to theobromine and 7-methylxanthine. The accumulation of 7-methylxanthine induced a premature equilibrium state and caused the remaining high concentration of theobromine. In the NdmA/NdmB mixture (Fig. 4c), caffeine consumption and theobromine production were changed to 84.56% and 121.94% compared to those of NdmAB (Fig. 4b). However, the amount of 7-methylxanthine was reduced by 47.01%, which was clearly below the NdmAB substrate conversion in the same experimental condition. Conclusively, NdmAB demonstrated the advantage of caffeine degradation with better efficiency than the simple mixture, which could be a driving force for the heterohexamerization of NdmA and NdmB under physiological conditions.

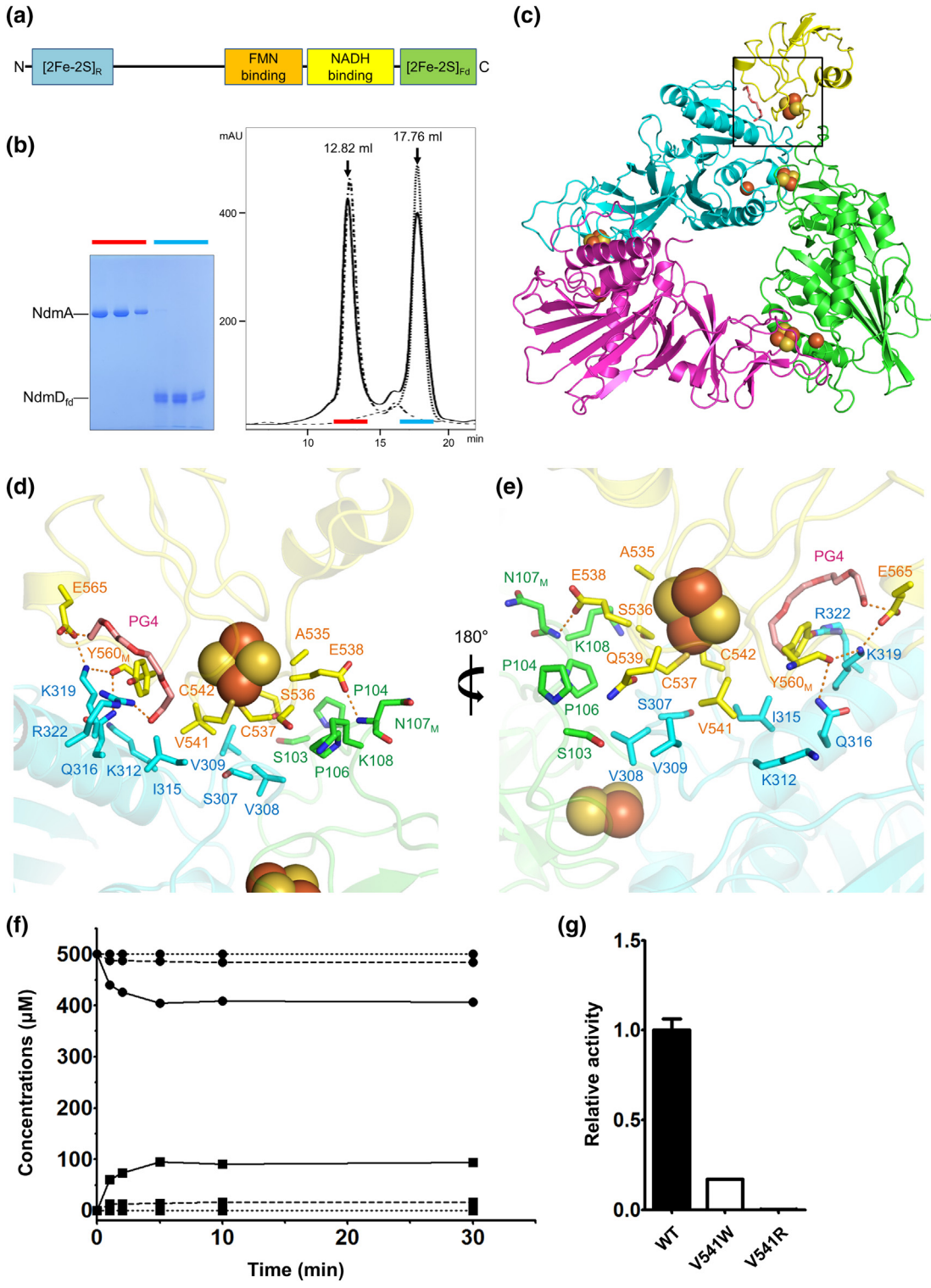

Complex structure of NdmA with the ferredoxin domain of NdmD

NdmD is the RO reductase that forms a stable ternary complex with NdmC and NdmE (NdmCDE). Since NdmC detaches the *N*-7 methyl group from methylxanthine derivatives, the NdmCDE complex is responsible for the last *N*-demethylation step of caffeine to xanthine (Fig. S1). However, NdmD is also needed by both NdmA and NdmB for electron transport from NADH to the oxygen activation site. Therefore, it is expected that transient interaction

would exist between them. NdmD is an FNR-type family and is classified as a type 1A reductase in the two-component system, which is composed of a FMN-binding domain, NADH-binding domain, and C-terminal plant-type ferredoxin domain (Fig. 5a). Remarkably, there is an additional Rieske domain at the N-terminus of NdmD [22], which is a unique feature compared with other RO reductases.

Previously, another RO structure, carbazole 1,9*a*-dioxygenase (CARDO) from *Janthinobacterium* sp. J3, was solved with the Rieske-type ferredoxin of *Pseudomonas resinovorans* CA10 [6]. According to the structure, the ferredoxin is located at the interface of two CARDO subunits, and the distance between [2Fe–2S] clusters was approximately 12–13 Å, which is suitable for electron transfer (Fig. S12a). Similarly, NdmA and NdmB could receive electrons from the C-terminal ferredoxin domain of NdmD. To obtain a binary complex of NdmA and the ferredoxin domain of NdmD (residues 499–588, referred to as $NdmD_{fd}$), the mixture was incubated for 30 min on ice, and size-exclusion chromatography was performed; however, they did not comigrate (Fig. 5b). Rather than purifying them together, we cocrystallized NdmA and $NdmD_{fd}$, and one condition in particular showed a different form of crystals compared with that of NdmA. The crystal was diffracted by 2.96 Å and a structural model of the NdmA–$NdmD_{fd}$ complex (referred to as $NdmAD_{fd}$) was built (Fig. 5c). This is the first reported complex structure of a plant-type ferredoxin domain, a part of type 1A reductase, with its physiological RO partner.

In the structure, $NdmD_{fd}$ interacted with two NdmA subunits at the oligomerization interface. Iron–sulfur cluster-coordinating C537 and C542, V541, A535, S536, and Q539 of $NdmD_{fd}$ formed a hydrophobic interface with K312, I315, V309, S307, and V308 of one NdmA subunit, and S103, P104, and P106 of another NdmA subunit. E538 of $NdmD_{fd}$ created a hydrogen bond with the main chain of N107 of NdmA (Fig. 5d,e). Q316 and K319 residues on the α7 helix of NdmA formed an interaction network with E565 and the main chain of Y560 of $NdmD_{fd}$. A linear extra electron density map was observed near the binding interface of $NdmAD_{fd}$ (Fig. S12b) and was determined as a tetra-ethylene glycol (PG4) derived from crystallization conditions. It formed hydrogen bonds with E565 of $NdmD_{fd}$ and R322 of NdmA.

The structure showed that only one $NdmD_{fd}$ bound to an NdmA trimer, while the remaining sites were empty. When we generated symmetry mates, another $NdmD_{fd}$ derived from the symmetry equivalent accessed one of these empty sites in the reverse orientation (Fig. S12c). To validate the $NdmAD_{fd}$ structure, V541 of $NdmD_{fd}$ located at the center of the $NdmAD_{fd}$ interface was mutated to a bulky hydrophobic residue, Trp (V541 W), or a highly flexible positively charged residue, Arg (V541R). Since the full-length NdmD protein was marginally soluble, we fused maltose-binding protein (MBP) at the N-terminus of the WT or mutant NdmD protein. Then, with MBP-NdmD, the caffeine degradation activity of NdmA was measured by HPLC analysis. Compared to the WT NdmD protein, the mutants showed reduced *N*-demethylase activity of less than 20% in V541W or almost negligible in V541R (Fig. 5f, g). Thus, the mutations appeared to reduce electron transport from NADH to the Rieske cluster of NdmA through a reduced interaction with $NdmD_{fd}$. From the results, we could consider that the $NdmAD_{fd}$ complex structure is physiologically relevant.

Mode of action of the *N*-demethylase complex

The hexameric structural arrangement and high sequence identity of NdmA and NdmB enable generation of the heterohexamer model of NdmAB, which has never been previously reported as an RO oligomerization state (Fig. 6a). The α3α′3 heterohexamer is expected to be energetically more favorable than the NdmA or NdmB homohexamer via a larger interface area [32]. The area of dimerized subunits from NdmA hexamer was 436.9 $Å^2$, involving 13 residues; for NdmB, the area was 463.6 $Å^2$, involving 15 residues. Moreover, within the α3α′3 heterohexamer model, the area was 585.3 $Å^2$, involving 18 residues. As shown in Fig. 6a, the caffeine molecule was initially recognized by the lateral direction of the NdmAB complex, which was perpendicular to 3-fold axis. The invisible loop in the apo structure possessed sufficient flexibility for accommodating the incoming substrate, caffeine

Fig. 5. Crystal structure of the $NdmAD_{fd}$ binary complex and reductase assay of NdmD. (a) Domain architecture of NdmD. Subscripts R and Fd indicate the Rieske-type and plant-type ferredoxin, respectively. The flavin mononucleotide (FMN)-binding region and nicotinamide adenine dinucleotide (NADH)-binding region are predicted in the middle (orange and yellow, respectively). (b) SEC profile and SDS-PAGE results for the NdmA–$NdmD_{fd}$ mixture (solid line). In comparison to the profiles of NdmA (12.82 mL) and $NdmD_{fd}$ (17.76 mL), the retention time of $NdmAD_{fd}$ mixture did not change. (c) Overall structure of the $NdmAD_{fd}$ binary complex. For clarity, only trimeric NdmA is shown (green, cyan, and magenta). The interface with $NdmD_{fd}$ (yellow) is magnified in panels d and e. (d, e) Front- and back-side views of the $NdmAD_{fd}$ interface with interacting residues. Hydrogen bonds are shown as orange dotted lines, and the residues with main chain interactions are indicated by subscript M. (f) HPLC analysis for caffeine (●) consumption and theobromine (■) production by NdmA in the presence of MBP-NdmD. WT NdmD produced 94.0 ± 10.8 μM (— line) of theobromine, V541W produced 16.0 ± 0.15 μM (- - - line), and V541R was not detectable (• • • • line). (g) Bar graphs of the relative activities for WT (black), V541W (white), and V541R (gray) of MBP-NdmD. Data represent the mean ± SEM of three independent experiments.

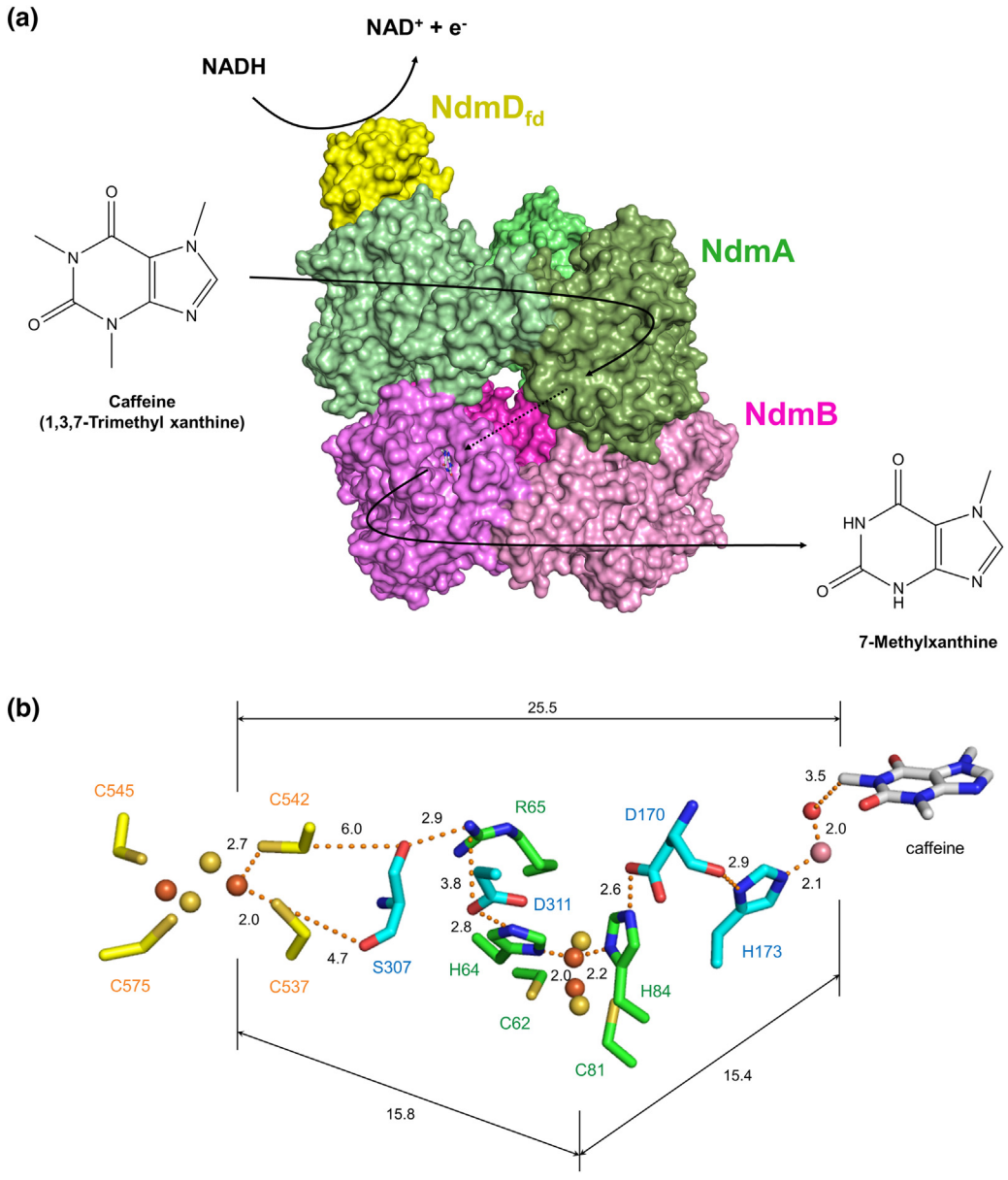

Fig. 6. Substrate and electron transfer pathway of the *N*-demethylase complex. (a) A model of the $NdmD_{fd}$–NdmA–NdmB complex. Greenish colored trimeric NdmA exhibits the closed conformation, and the bound caffeine molecules are shown in the surface representation; in contrast, the bound theobromine molecule is shown in the pinkish trimeric NdmB ($NdmA_{QL}$ mutant). The orientation and position of the NdmCDE complex can be speculated based on our complex structure between NdmA and NdmDfd (yellow). (b) Electron transfer pathway from the ferredoxin domain of NdmD to caffeine in the catalytic site of NdmA. The plant-type [2Fe–2S] cluster in the ferredoxin domain is coordinated by four cysteine residues (yellow) facing the subunit interface of NdmA, which is colored blue for the SRPBCC domain of one subunit and green for the Rieske domain of another subunit. Since an excess amount of cobalt was used for the NdmA-caffeine complex structure, a cobalt ion (salmon sphere) is displayed instead of a nonheme iron ion. A water molecule from the nonheme iron center is possibly replaced with an oxygen molecule for *N*-demethylation. All distances are presented in angstroms, and residues involved in electron transfer are connected with orange dotted lines.

(Fig. S3e); then, the *N*-demethylation reaction occurred in the closed conformation (Figs. 2b and S6a). The product of the theobromine-releasing pathway was not clear from the current structure of NdmA; however, the enzymatic product of NdmA did not need to dissociate completely and then rebind to the active site of NdmB by a diffusion-controlled reaction. Instead, the neighboring NdmB could easily recognize the product and efficiently degrade it to 7-methylxanthine, a substrate of NdmC.

We speculate that the same scenario must be applied to the relationship between NdmB and NdmC. NdmC is one of the components of the NdmCDE heterotrimer, and its functional Rieske domain may exist on the NdmD protein. We dissected the interaction between the ferredoxin domain of NdmD, Ndm_{fd}, and NdmA, which exhibited very transient binding and, most likely, the same characteristics as those observed between Ndm_{fd} and NdmB. Based on our NdmA–$NdmD_{fd}$ complex structure, the electron transport pathway from the ferredoxin domain to the *N*-demethylation site of caffeine is now elucidated (Fig. 6b). The plant-type [2Fe–2S] cluster in $NdmD_{fd}$ was coordinated by four cysteine residues: C537, C542, C545, and C575. C542 and C537 face the oligomerization interface of the NdmA subunits, which was formed by the SRPBCC domain of one subunit and the Rieske domain of another subunit. The direct distance from the plant-type [2Fe–2S] cluster to the *N*-demethylation site was 25.5 Å, but along the electron transfer pathway, it was 15.8 Å from the NdmD plant-type [2Fe–2S] cluster to the Rieske cluster of NdmA and 15.4 Å from the Rieske cluster to the *N*-demethylation site (Fig. 6b). Furthermore, simple superposition of NdmA from the $NdmAD_{fd}$ binary complex and the NdmAB hexamer clearly showed a potential orientation and position of the NdmCDE complex (Fig. 6a), although it is still unclear how hexameric NdmAB interacts with the NdmCDE complex.

The detailed *N*-demethylation mechanism was further investigated by substrate complex structures with NdmA and NdmB. The distance between the *N*-methyl group and nonheme iron is important for regio-specific *N*-demethylation by NdmA and NdmB. Based our structure-based mutagenesis, the $NdmA_{QL}$ (plus loop swapped) mutant clearly mimicked NdmB activity with the NdmA backbone (Fig. S8). As described in Introduction, metabolites of caffeine, especially paraxanthine (1,7-dimethylxanthine), are extremely useful for industrial applications. Our high-resolution structures in combination with biochemical assays will provide excellent guidance for rational protein engineering. An enzymatically competent NdmB mutant recognizing caffeine or a NdmA mutant possessing N_3-demethylation activity will be highly valuable because paraxanthine is very expensive and currently manufactured through multistep chemical synthesis. Only 2%–3% of the caffeine is converted to paraxanthine by caffeine-degrading bacteria [33]. Therefore, this study provides a framework for generating mutants with altered enzymatic activity for caffeine degradation, facilitating further engineering of bacterial strains. These findings will contribute to potential applications to produce biofuels, animal feed, and pharmaceuticals from coffee and tea waste.

Materials and Methods

Cloning, expression, and purification

PCR-amplified full-length *ndmA* and *ndmB* were subcloned into pETDuet-1 (Novagen) vectors with N-terminal hexahistidine (His_6) tags, and the plasmids were transformed into competent *Escherichia coli* BL21(DE3) cells. Protein overexpression was induced when the OD600 reached 0.5–0.8 with 0.5 mM IPTG and 1 mM $Fe(II)SO_4$ at 18 °C for 18 h. Cells were harvested by centrifugation at 6300*g* for 15 min and resuspended in buffer A [20 mM Hepes–NaOH (pH 7.5), 300 mM NaCl, and 1 mM TCEP]. The resuspended cells were disrupted by sonication in the presence of 1 mM PMSF and protease inhibitor cocktail, and then clarified by centrifugation at 27,200*g* for 1 h. The filtered supernatant fraction was loaded onto a HisTrap™ (GE Healthcare) and eluted by gradually increasing the concentration of imidazole up to 500 mM in 20 mM Hepes–NaOH (pH 7.5), 100 mM NaCl, and 1 mM TCEP. Further purification was performed using an ion-exchange chromatography column, HiTrap™ Q FF (GE Healthcare) and eluted with an increasing concentration of NaCl. The eluent was finally loaded on a HiLoad™ 16/600 Superdex™ 200 pg (GE Healthcare) gel filtration column pre-equilibrated with 10 mM Hepes–NaOH (pH 7.5) containing 150 mM NaCl and 1 mM TCEP.

For MBP-NdmD, PCR amplified *ndmD* was subcloned into the pMAL-c2X (New England BioLabs) vector with an N-terminal MBP tag. For mutagenesis, the QuikChange site-directed mutagenesis protocol (Stratagene) with Pfu DNA polymerase was used. Plasmid transformation and overexpression methods for MBP-NdmD were the same as previously described. For the affinity purification step, the clarified MBP-NdmD lysate was loaded onto amylose resin (New England BioLabs) and eluted with 10 mM maltose containing buffer A. Ion-exchange chromatography and size-exclusion chromatography steps were the same as for the other proteins. NdmCDE and NdmCDE H120A/D237A overexpression methods were the same as previously described herein. Before size-exclusion chromatography, 2 mM of NADH and FMN was added to the protein solution, followed by incubation on ice for 30 min. For fluorescence protein-labeled constructs, PCR-amplified mCherry and ECFP from the original templates (Clontech) were subcloned into a laboratory-modified pRSF vector (Novagen), which already contained NdmA and NdmB, respectively. The complete versions of constructs were His_6-mCherry-NdmA and His_6-ECFP-NdmB. Protein expression and purification steps were the same as those used for His_6-NdmA and His6-NdmB. All protein samples were confirmed by SDS-PAGE.

Crystallization and data collection

The purified NdmA or NdmB was concentrated to 12–17 mg/mL and crystallized at 20 °C using the sitting drop vapor diffusion method. Initial crystals of NdmA were obtained with 0.2 M ammonium citrate/citric acid (pH 7.5), 15% (w/v) PEG 3350, and 20% (v/v) 2-propanol within 1 day. The optimized crystal was obtained by mixing 1 μL of protein and 1 μL of reservoir solution containing 15%–17% (w/v) PEG 3350 and 17%–20% (v/v) 2-propanol. The crystal of NdmB was first obtained with 0.1 M Tris–HCl (pH 8.5), 0.5 M NaCl, 5.36% (w/v) PEG 8000, and 20.1% (v/v) MPD within 1 day. The optimized crystal was obtained within the variation of 6%–8% (w/v) PEG 8000 and 16%–17% (v/v) MPD. All crystals were flash-frozen in liquid nitrogen by adding 15% (w/v) glycerol to the original condition as a cryo-protectant. To obtain substrate-bound crystals, 1 μL of 1–5 mM of caffeine, 1–5 mM of theophylline, or 1–10 mM theobromine solution was incubated with the NdmA or NdmB crystal for 1 day. To inhibit the enzyme activity of NdmA or NdmB, an excess amount of cobalt (II) was added to replace the nonheme iron ion. To prevent substrate release, the same amount of chemicals was added to the cryo-solution while being flash-frozen. For $NdmAD_{fd}$ complex crystallization, 8 mg/mL of the NdmA and NdmDfd mixture with a 1:1.5 molar ratio was applied for cocrystallization. The initial crystallization conditions were 0.1 M Bicine/Tris (pH 8.5), 0.02 M monosaccharides, 10% (w/v) PEG 20,000, and 20% (v/v) PEG MME 500; the optimized crystals were obtained with 7%–8% (w/v) PEG 20,000 and 16%–18% (v/v) PEG MME 500. The crystals were flash-frozen in liquid nitrogen by addition of 10% (w/v) glycerol as a cryo-protectant.

The Fe-multiwavelength anomalous dispersion (Fe-MAD) data for NdmB were collected at the BL17A beamline of the Photon Factory, Japan, and other native and substrate-bound complex data were collected at the 5C beamline of the Pohang Accelerator Laboratory, Korea. $NdmAD_{fd}$ data were collected at the BL44XU beamline of SPring-8, Japan. Data indexing, integration, and scaling were performed using HKL2000 software [34]. Table S2 summarizes the statistics for the collected data.

Structure determination and refinement

By calculation using the Fe-MAD data for NdmB, five anomalous scatterer sites were identified, four sites from the Rieske [2Fe–2S] cluster and 1 site from the nonheme iron center [35,36]. Ten fragmented chains were initially built by automatic model building and manually rebuilt using COOT [36,37]. With the model, molecular replacement (MR) of native NdmB was performed using Phaser [38] and refined using phenix.refine [39]. The initial phase of NdmA was obtained by MR with the native NdmB structure and subjected to AutoBuild and phenix.refine. All the substrate-bound structures for NdmA and $NdmA_{QL}$ were solved by MR with the apo NdmA structure. The $NdmAD_{fd}$ complex structure was determined by MR with the NdmA structure, but the ferredoxin domain of NdmD was manually built using COOT. Structural comparisons were performed using the DALI server [40], and all structural figures were drawn using PyMOL (http://www.pymol.org).

Fluorescence measurements

Purification of the coexpressed mCherry-NdmA/NdmB or mCherry-NdmA/ECFP-NdmB was performed with the typical chromatography steps as described above. After the samples were loaded on a HiLoad™ 16/600 Superdex™ 200-pg gel filtration column, the eluents were fractionated by every 1.5 mL of retention volume. Then, 200 μL of each sample was transferred to 96-well black/clear bottom microplates, and the fluorescence signals were measured using a SpectraMax M5 (Molecular Devices). Previously, the excitation/emission wavelengths of the pure mCherry-NdmA and ECFP-NdmB were designated as 590/620 nm (610-nm cutoff) and 440/480 nm (470-nm cutoff) by spectrum scanning, respectively. The results were generated by using SoftMax Pro 6 (Molecular Devices) and quantified with standard curves of both mCherry-NdmA and ECFP-NdmB.

Small-angle x-ray scattering

For the SAXS experiment coupled with size-exclusion chromatography column (SEC-SAXS), protein samples (NdmA, NdmB, and NdmAB) were concentrated to 9.7–21.6 mg/mL, and 100 μL of each sample was injected into a Superdex™ 200 Increase 10/300 GL column (GE Healthcare) pre-equilibrated with buffer B [25 mM Hepes (pH 7.5), 150 mM NaCl, 2 mM TCEP, and 10% (w/v) glycerol]. The flow rate was changed from 0.5 to 0.05 mL/min, depending on the sample elution. The data were collected at Beamline BL-10C, Photon Factory, Japan. PILATUS3 2 M (DECTRIS) was used as the x-ray detector. The wavelength was 1.5 Å with a 10-s exposure, and the sample-detector distance was 3 m. Conventional static SAXS experiments were performed for NdmAB, mCherry-NdmA/NdmB, and mCherry-NdmA/ECFP-NdmB with the same buffer conditions described above. The 10–11 mg/mL of protein samples was serially diluted from 100% to 40% concentration. All scattering data were measured at Beamline 4C, Pohang Accelerator Laboratory, Korea. Rayonix 2D SX165 (Rayonix) was used as the x-ray detector. Data were collected with a 5-s exposure using a wavelength of 0.733 Å, and two-distance data of 4 and 2 m were

merged. Data from the detector were normalized, averaged, buffer-subtracted, and placed on an absolute scale relative to water according to standard procedures with an in-house program. Raw data from SEC-SAXS were processed by CHROMIXS [41] and subjected to analysis with the software package PRIMUS [42], which provided the radius of gyration (Rg), Porod volume, and experimental molecular weight. An indirect Fourier transform of the scattering curve $I(s)$ calculated by GNOM was used to obtain the distance distribution function $P(r)$ and the maximum particle dimensions Dmax [43]. The theoretical scattering curves calculated from the crystal structure were compared with the experimental scattering curves using CRYSOL [44]. *Ab initio* modeling and averaging of these models were performed using DAMMIF [45] and DAMAVER [46], respectively. SAXS electron envelopes from the *ab initio* DAMMIF model were generated using Chimera [47]. Table S1 summarizes the statistics for the SEC-SAXS and static-SAXS experiments.

SEC-MALS

SEC-MALS experiments were performed using an Äkta FPLC system (GE Healthcare) coupled with Wyatt MiniDAWN TREOS (Wyatt Technology). The protein samples (NdmA, NdmB, and NdmAB) were loaded onto a Superdex™ 200 Increase 10/300 GL gel filtration column using buffer B. Bovine serum albumin was used as the isotropic scatterer for detector normalization. Light scattering was measured and analyzed using ASTRA V software (Wyatt Technology).

Enzyme activity assays

The enzyme activity assay has been well described in the previous study by Summers *et al*. [22]. Briefly, NADH:cytochrome *c* oxidoreductase activity was determined in a 1 mL reaction with 50 mM potassium phosphate buffer (pH 7.5) containing 300 μM NADH, 87 μM equine cytochrome *c*, and 0.2 μg of purified MBP-NdmD. The activity was monitored by absorbance at 550 nm at 30 °C and quantified with an extinction coefficient of 21,000 M^{-1} cm^{-1} for oxidized cytochrome *c*. One unit of activity was defined as 1 μmol of cytochrome *c* reduced per min. NdmA and NdmB kinetics assays contained, in a 0.5-mL total volume, 0.5 mM methylxanthine, 0.5 mM NADH, 50 μM $Fe(NH_4)_2(SO_4)_2$, and 2.5 μg of His_6-NdmA or His_6-NdmB in 50 mM potassium phosphate buffer (pH 7.5). Approximately 120 U of purified MBP-NdmD was added to the reaction mixture. The reaction mixture was incubated at 30 °C with shaking at 300 rpm on a microtube shaker. Periodically, 80 μL of the samples from the reaction mixture was mixed with an equal volume of acetonitrile to quantify the concentrations of methylxanthines and *N*-demethylated products by HPLC. To test the activity of MBP-NdmD V541W and V541R mutants, the same amounts of mutant proteins as WT MBP-NdmD were used under the same assay conditions. For the methylxanthine *N*-demethylase activity assays, the 0.5-mL reaction solution contained 0.5 mM caffeine, 2 mM NADH, 50 μM $Fe(NH_4)_2(SO_4)_2$, and 50 μg of His_6-NdmAB or a mixture of His_6-NdmA and His_6-NdmB in 50 mM potassium phosphate buffer (pH 7.5). Approximately 120 U of WT or mutant NdmCDE was used, and the sampling method for HPLC analysis was the same as described above.

HPLC analysis

Quantifications of caffeine, theobromine, 7-methylxanthine, and xanthine were conducted with a Waters 515 HPLC system equipped with an Autosampler 717 and photodiode array detector connected to a Hypersil BDS C18 column (4.6 mm by 125 mm, Thermo Fisher Scientific). For analysis, methanol–water (18:82, v/v) was used as an isocratic mobile phase at a flow rate of 0.5 mL/min.

Accession codes

Coordinates and structure factors for the crystal structures solved in this work have been deposited in the Protein Data Bank under accession codes 6ICK, 6ICL, 6ICM, 6ICN, 6ICO, 6ICP, and 6ICQ. The models and scattering curves for SAXS study were deposited in the SASDB with IDs: SASDFD7, SASDFE7, SASDFF7, SASDFG7, SASDFH7, and SASDFJ7.

Acknowledgments

We thank the staff at Beamlines 5C and 11C, Pohang Accelerator Laboratory, Korea and Beamline BL17A, Photon Factory, Japan, for help with the x-ray data collection. This work was performed in part under the International Collaborative Research Program of the Institute for Protein Research, Osaka University (ICR-17-05). Diffraction data were collected at Osaka University Beamline BL44XU at SPring-8 (Harima, Japan) (Proposal No. 2018B6867). We also thank the staff at Beamline 4C, Pohang Accelerator Laboratory, Korea, and Beamline BL10C, Photon Factory, Japan, for help with the SAXS data collection. This work was supported by National Research Foundation of Korea (NRF) grants from the Korean government (2016R1E1A1A01942623), Korea University Future

Research Grant (K1822321), US National Science Foundation (NSF) East Asia Pacific Summer Institute Fellowship (No. 1713935), and University of Alabama research funds.

Author Contributions

J.H.K. contributed to the cloning, purification, crystallization, structural analysis, enzyme activity assays, and SAXS and MALS analysis; B.H.K. contributed to the SAXS data collection and analysis; S.B. and R.M.S. contributed to the design and analysis of the enzyme activity assays; S.Y.K. contributed to the purification and crystallization; J. H.K. and H.K.S. designed the research and wrote the manuscript.

Declaration of Competing Interest

The authors declare that they have no conflicts of interest.

Appendix A. Supplementary data

Supplementary data to this article can be found online at https://doi.org/10.1016/j.jmb.2019.08.004.

Received 20 June 2019;
Received in revised form 2 August 2019;
Accepted 6 August 2019
Available online 11 August 2019

Keywords:
caffeine;
N-demethylase;
plant-type ferredoxin;
rational protein engineering;
reductase

Abbreviations:
buffer A, 20 mM Hepes–NaOH (pH 7.5), 300 mM NaCl, and 1 mM TCEP; buffer B, 25 mM Hepes (pH 7.5), 150 mM NaCl, 2 mM TCEP, and 10% (w/v) glycerol; CARDO, carbazole 1,9*a*-dioxygenase; FMN, flavin mononucleotide; His_6, hexahistidine; MAD, multiwavelength anomalous dispersion; MBP, maltose-binding protein; MR, molecular replacement; NdmAB, a complex between NdmA and NdmB; $NdmAD_{fd}$, NdmA–$NdmD_{fd}$ complex; $NdmA_{QL}$, a mutant NdmA that imitated the catalytic site of NdmB; $NdmD_{fd}$, a ferredoxin domain of NdmD; RO, Rieske nonheme iron oxygenase; SAXS, small-angle x-ray scattering; SEC-MALS, size-exclusion chromatography with a multi-angle light scattering; SRPBCC, *S*TART/*R*HO_alpha_C/*P*ITP/*B*et_v1/*C*oxG/*C*alC domain; WT, wild-type.

References

[1] R.H. Peng, A.S. Xiong, Y. Xue, X.Y. Fu, F. Gao, W. Zhao, et al., Microbial biodegradation of polyaromatic hydrocarbons, FEMS Microbiol. Rev. 32 (2008) 927–955.
[2] A.K. Haritash, C.P. Kaushik, Biodegradation aspects of polycyclic aromatic hydrocarbons (PAHs): a review, J. Hazard. Mater. 169 (2009) 1–15.
[3] S.K. Samanta, O.V. Singh, R.K. Jain, Polycyclic aromatic hydrocarbons: environmental pollution and bioremediation, Trends Biotechnol. 20 (2002) 243–248.
[4] D.J. Ferraro, L. Gakhar, S. Ramaswamy, Rieske business: structure–function of Rieske non-heme oxygenases, Biochem. Biophys. Res. Commun. 338 (2005) 175–190.
[5] L.P. Wackett, Mechanism and applications of Rieske non-heme iron dioxygenases, Enzym. Microb. Technol. 31 (2002) 577–587.
[6] K. Inoue, Y. Usami, Y. Ashikawa, H. Noguchi, T. Umeda, A. Yamagami-Ashikawa, et al., Structural basis of the divergent oxygenation reactions catalyzed by the rieske nonheme iron oxygenase carbazole 1,9*a*-dioxygenase, Appl. Environ. Microbiol. 80 (2014) 2821–2832.
[7] R.L. D'Ordine, T.J. Rydel, M.J. Storek, E.J. Sturman, F. Moshiri, R.K. Bartlett, et al., Dicamba monooxygenase: structural insights into a dynamic Rieske oxygenase that catalyzes an exocyclic monooxygenation, J. Mol. Biol. 392 (2009) 481–497.
[8] A. Karlsson, J.V. Parales, R.E. Parales, D.T. Gibson, H. Eklund, S. Ramaswamy, Crystal structure of naphthalene dioxygenase: side-on binding of dioxygen to iron, Science. 299 (2003) 1039–1042.
[9] Y. Furusawa, V. Nagarajan, M. Tanokura, E. Masai, M. Fukuda, T. Senda, Crystal structure of the terminal oxygenase component of biphenyl dioxygenase derived from *Rhodococcus* sp. strain RHA1, J. Mol. Biol. 342 (2004) 1041–1052.
[10] A. Kumari, D. Singh, S. Ramaswamy, G. Ramanathan, Structural and functional studies of ferredoxin and oxygenase components of 3-nitrotoluene dioxygenase from *Diaphorobacter* sp. strain DS2, PLoS One 12 (2017), e0176398.
[11] R. Dumitru, W.Z. Jiang, D.P. Weeks, M.A. Wilson, Crystal structure of dicamba monooxygenase: a Rieske nonheme oxygenase that catalyzes oxidative demethylation, J. Mol. Biol. 392 (2009) 498–510.
[12] Y. Hurtubise, D. Barriault, M. Sylvestre, Involvement of the terminal oxygenase beta subunit in the biphenyl dioxygenase reactivity pattern toward chlorobiphenyls, J. Bacteriol. 180 (1998) 5828–5835.
[13] C.L. Colbert, N.Y.R. Agar, P. Kumar, M.N. Chakko, S.C. Sinha, J.B. Powlowski, et al., Structural characterization of *Pandoraea pnomenusa* B-356 biphenyl dioxygenase reveals features of potent polychlorinated biphenyl-degrading enzymes, PLoS One 8 (2013).
[14] J. Hirose, A. Suyama, S. Hayashida, K. Furukawa, Construction of hybrid biphenyl (Bph) and toluene (Tod) genes for functional-analysis of aromatic ring dioxygenases, Gene. 138 (1994) 27–33.
[15] Q. Chen, C.H. Wang, S.K. Deng, Y.D. Wu, Y. Li, L. Yao, et al., Novel three-component Rieske non-heme iron oxygenase system catalyzing the *N*-dealkylation of chloroacetanilide herbicides in sphingomonads DC-6 and DC-2, Appl. Environ. Microbiol. 80 (2014) 5078–5085.

[16] A.M. Jeffrey, H.J. Yeh, D.M. Jerina, T.R. Patel, J.F. Davey, D. T. Gibson, Initial reactions in the oxidation of naphthalene by *Pseudomonas putida*, Biochemistry. 14 (1975) 575–584.
[17] R.E. Parales, K. Lee, S.M. Resnick, H. Jiang, D.J. Lessner, D.T. Gibson, Substrate specificity of naphthalene dioxygenase: effect of specific amino acids at the active site of the enzyme, J. Bacteriol. 182 (2000) 1641–1649.
[18] R.E. Parales, S.M. Resnick, C.L. Yu, D.R. Boyd, N.D. Sharma, D. T. Gibson, Regioselectivity and enantioselectivity of naphthalene dioxygenase during arene cis-dihydroxylation: control by phenylalanine 352 in the alpha subunit, J. Bacteriol. 182 (2000) 5495–5504.
[19] F.J. Mondello, M.P. Turcich, J.H. Lobos, B.D. Erickson, Identification and modification of biphenyl dioxygenase sequences that determine the specificity of polychlorinated biphenyl degradation, Appl. Environ. Microbiol. 63 (1997) 3096–3103.
[20] C.L. Yu, T.M. Louie, R. Summers, Y. Kale, S. Gopishetty, M. Subramanian, Two distinct pathways for metabolism of theophylline and caffeine are coexpressed in *Pseudomonas putida* CBB5, J. Bacteriol. 191 (2009) 4624–4632.
[21] R.M. Summers, T.M. Louie, C.L. Yu, M. Subramanian, Characterization of a broad-specificity non-haem iron *N*-demethylase from *Pseudomonas putida* CBB5 capable of utilizing several purine alkaloids as sole carbon and nitrogen source, Microbiology. 157 (2011) 583–592.
[22] R.M. Summers, T.M. Louie, C.L. Yu, L. Gakhar, K.C. Louie, M. Subramanian, Novel, highly specific *N*-demethylases enable bacteria to live on caffeine and related purine alkaloids, J. Bacteriol. 194 (2012) 2041–2049.
[23] R.M. Summers, J.L. Seffernick, E.M. Quandt, C.L. Yu, J.E. Barrick, M.V. Subramanian, Caffeine junkie: an unprecedented glutathione *S*-transferase-dependent oxygenase required for caffeine degradation by *Pseudomonas putida* CBB5, J. Bacteriol. 195 (2013) 3933–3939.
[24] R.G. Hollingsworth, J.W. Armstrong, E. Campbell, Caffeine as a repellent for slugs and snails, Nature. 417 (2002) 915–916.
[25] J.A. Nathanson, Caffeine and related methylxanthines: possible naturally occurring pesticides, Science. 226 (1984) 184–187.
[26] A. Lelo, D.J. Birkett, R.A. Robson, J.O. Miners, Comparative pharmacokinetics of caffeine and its primary demethylated metabolites paraxanthine, theobromine and theophylline in man, Br. J. Clin. Pharmacol. 22 (1986) 177–182.
[27] W. Wan, D. Cui, K. Trier, J. Zeng, Effect of 7-methylxanthine on human retinal pigment epithelium cells cultured in vitro, Mol. Vis. 23 (2017) 1006–1014.
[28] S. Guerreiro, D. Toulorge, E. Hirsch, M. Marien, P. Sokoloff, P.P. Michel, Paraxanthine, the primary metabolite of caffeine, provides protection against dopaminergic cell death via stimulation of ryanodine receptor channels, Mol. Pharmacol. 74 (2008) 980–989.
[29] J.S. Penfield, L.J. Worrall, N.C. Strynadka, L.D. Eltis, Substrate specificities and conformational flexibility of 3-ketosteroid 9 alpha-hydroxylases, J. Biol. Chem. 289 (2014) 25523–25536.
[30] B.M. Martins, T. Svetlitchnaia, H. Dobbek, 2-Oxoquinoline 8-monooxygenase oxygenase component: active site modulation by Rieske-[2Fe–2S] center oxidation/reduction, Structure. 13 (2005) 817–824.
[31] Ferraro DJ, Brown EN, Yu CL, Parales RE, Gibson DT, Ramaswamy S. Structural investigations of the ferredoxin and terminal oxygenase components of the biphenyl 2,3-dioxygenase from Sphingobium yanoikuyae B1. BMC Struct Biol. 2007;7:10.
[32] E. Krissinel, K. Henrick, Inference of macromolecular assemblies from crystalline state, J. Mol. Biol. 372 (2007) 774–797.
[33] S.S. Dash, S.N. Gummadi, Catabolic pathways and biotechnological applications of microbial caffeine degradation, Biotechnol. Lett. 28 (2006) 1993–2002.
[34] Z. Otwinowski, W. Minor, Processing of x-ray diffraction data collected in oscillation mode, Methods Enzymol. 276 (1997) 307–326.
[35] P.D. Adams, P.V. Afonine, G. Bunkoczi, V.B. Chen, I.W. Davis, N. Echols, et al., PHENIX: a comprehensive Python-based system for macromolecular structure solution, Acta Crystallogr D Biol Crystallogr. 66 (2010) 213–221.
[36] T.C. Terwilliger, R.W. Grosse-Kunstleve, P.V. Afonine, N.W. Moriarty, P.H. Zwart, L.W. Hung, et al., Iterative model building, structure refinement and density modification with the PHENIX AutoBuild wizard, Acta Crystallogr D Biol Crystallogr. 64 (2008) 61–69.
[37] P. Emsley, B. Lohkamp, W.G. Scott, K. Cowtan, Features and development of Coot, Acta Crystallogr D Biol Crystallogr. 66 (2010) 486–501.
[38] A.J. McCoy, R.W. Grosse-Kunstleve, P.D. Adams, M.D. Winn, L.C. Storoni, R.J. Read, Phaser crystallographic software, J. Appl. Crystallogr. 40 (2007) 658–674.
[39] P.V. Afonine, R.W. Grosse-Kunstleve, N. Echols, J.J. Headd, N.W. Moriarty, M. Mustyakimov, et al., Towards automated crystallographic structure refinement with phenix.refine, Acta Crystallogr D Biol Crystallogr. 68 (2012) 352–367.
[40] L. Holm, L.M. Laakso, Dali server update, Nucleic Acids Res. 44 (2016) W351–W355.
[41] A. Panjkovich, D.I. Svergun, CHROMIXS: automatic and interactive analysis of chromatography-coupled small-angle x-ray scattering data, Bioinformatics. 34 (2018) 1944–1946.
[42] P.V. Konarev, V.V. Volkov, A.V. Sokolova, M.H.J. Koch, D.I. Svergun, PRIMUS: a Windows PC-based system for small-angle scattering data analysis, J. Appl. Crystallogr. 36 (2003) 1277–1282.
[43] D.I. Svergun, Determination of the regularization parameter in indirect-transform methods using perceptual criteria, J. Appl. Crystallogr. 25 (1992) 495–503.
[44] D. Svergun, C. Barberato, M.H.J. Koch, CRYSOL—a program to evaluate x-ray solution scattering of biological macromolecules from atomic coordinates, J. Appl. Crystallogr. 28 (1995) 768–773.
[45] D. Franke, D.I. Svergun, DAMMIF, a program for rapid ab-initio shape determination in small-angle scattering, J. Appl. Crystallogr. 42 (2009) 342–346.
[46] V.V. Volkov, D.I. Svergun, Uniqueness of ab initio shape determination in small-angle scattering, J. Appl. Crystallogr. 36 (2003) 860–864.
[47] E.F. Pettersen, T.D. Goddard, C.C. Huang, G.S. Couch, D.M. Greenblatt, E.C. Meng, et al., UCSF Chimera—a visualization system for exploratory research and analysis, J. Comput. Chem. 25 (2004) 1605–1612.